1-1-2019

Defect-Induced Pt-Co-Se Coordinated Sites with Highly Asymmetrical Electronic Distribution for Boosting Oxygen-Involving Electrocatalysis

Linzhou Zhuang
University of Queensland

Yi Jia
Griffith University

Hongli Liu
Qingdao University

Xin Wang
Griffith University

Rosalie K. Hocking
Swinburne University of Technology

See next page for additional authors

Defect-Induced Pt-Co-Se Coordinated Sites with Highly Asymmetrical Electronic Distribution for Boosting Oxygen-Involving Electrocatalysis

Abstract

Rational design and synthesis of hetero-coordinated moieties at the atomic scale can significantly raise the performance of the catalyst and obtain mechanistic insight into the oxygen-involving electrocatalysis. Here, a facile plasma-photochemical strategy is applied to construct atomically coordinated Pt-Co-Se moieties in defective CoSe2 (CoSe2−x) through filling the plasma-created Se vacancies in CoSe2−x with single Pt atomic species (CoSe2−x-Pt) under ultraviolet irradiation. The filling of single Pt can remarkably enhance the oxygen evolution reaction (OER) activity of CoSe2. Optimal OER specific activity is achieved with a Pt content of 2.25 wt% in CoSe2−x-Pt, exceeding that of CoSe2−x by a factor of 9. CoSe2−x-Pt shows much better OER performance than CoSe2−x filled with single Ni and even Ru atomic species (CoSe2−x-Ni and CoSe2−x-Ru). Noticeably, it is general that Pt is not a good OER catalyst but Ru is; thus the design of active sites for electrocatalysis at an atomic level should follow a different intrinsic mechanism. Mechanism studies unravel that the single Pt can induce much higher electronic distribution asymmetry degree than both single Ni and Ru, and benefit the interaction between the Co sites and adsorbates (OH*, O*, and OOH*) during the OER process, leading to a better OER activity.

Disciplines

Engineering | Physical Sciences and Mathematics

Publication Details

Zhuang, L., Jia, Y., Liu, H., Wang, X., Hocking, R. K., Liu, H., Chen, J., Ge, L., Zhang, L., Li, M., Dong, C., Huang, Y., Shen, S., Yang, D., Zhu, Z. & Yao, X. (2019). Defect-Induced Pt-Co-Se Coordinated Sites with Highly Asymmetrical Electronic Distribution for Boosting Oxygen-Involving Electrocatalysis. Advanced Materials, 31 (4), 1805581-1-1805581-10.

Authors

Linzhou Zhuang, Yi Jia, Hongli Liu, Xin Wang, Rosalie K. Hocking, Hongwei Liu, Jun Chen, Lei Ge, Longzhou Zhang, Mengran Li, Chung-Li Dong, Yu-Cheng Huang, Shaohua Shen, Dongjiang Yang, Zhonghua Zhu, and Xiangdong Yao

Defect-Induced Pt–Co–Se Coordinated Sites with Highly Asymmetrical Electronic Distribution for Boosting Oxygen-Involving Electrocatalysis

Linzhou Zhuang, Yi Jia, Hongli Liu, Xin Wang, Rosalie K. Hocking, Hongwei Liu, Jun Chen, Lei Ge, Longzhou Zhang, Mengran Li, Chung-Li Dong, Yu-Cheng Huang, Shaohua Shen, Dongjiang Yang, Zhonghua Zhu, and Xiangdong Yao**

Rational design and synthesis of hetero-coordinated moieties at the atomic scale can significantly raise the performance of the catalyst and obtain mechanistic insight into the oxygen-involving electrocatalysis. Here, a facile plasma-photochemical strategy is applied to construct atomically coordinated Pt–Co–Se moieties in defective $CoSe_2$ ($CoSe_{2-x}$) through filling the plasma-created Se vacancies in $CoSe_{2-x}$ with single Pt atomic species ($CoSe_{2-x}$-Pt) under ultraviolet irradiation. The filling of single Pt can remarkably enhance the oxygen evolution reaction (OER) activity of $CoSe_2$. Optimal OER specific activity is achieved with a Pt content of 2.25 wt% in $CoSe_{2-x}$-Pt, exceeding that of $CoSe_{2-x}$ by a factor of 9. $CoSe_{2-x}$-Pt shows much better OER performance than $CoSe_{2-x}$ filled with single Ni and even Ru atomic species ($CoSe_{2-x}$-Ni and $CoSe_{2-x}$-Ru). Noticeably, it is general that Pt is not a good OER catalyst but Ru is; thus the design of active sites for electrocatalysis at an atomic level should follow a different intrinsic mechanism. Mechanism studies unravel that the single Pt can induce much higher electronic distribution asymmetry degree than both single Ni and Ru, and benefit the interaction between the Co sites and adsorbates (OH*, O*, and OOH*) during the OER process, leading to a better OER activity.

Heterogeneous catalysts are appealing for their high activity and/or selectivity in industrial processes due to their tuneable atomic coordination structure at multi-phase (gas–liquid–solid) reaction site.[1,2] However, heterogeneous catalysts suffer from the low atom utilization efficiency because of their limited surface active sites accessible to reactants.[3] To address this challenge, considerable efforts have been devoted to downsizing the bulk heterocatalysts to low dimensional or even atomic scale that can maximize the exposed active sites.[3] Recently, atomically dispersed catalysts with isolated metal atoms on supports such as metal oxides,[4] carbides,[5] transition-metal dichalcogenides (TMDs),[6] zeolites,[7] and carbons[8] have sparked new interests in heterogeneous catalysis, and demonstrated excellent catalytic performance in water–gas

L. Zhuang, Dr. L. Ge, Dr. M. Li, Prof. Z. Zhu
School of Chemical Engineering
the University of Queensland
Brisbane 4072, Australia
E-mail: z.zhu@uq.edu.au
Dr. Y. Jia, Dr. X. Wang, Dr. L. Zhang, Prof. X. Yao
School of Environment and Sciences, and Queensland Micro- and Nanotechnology Centre
Griffith University
Nathan Campus, Nathan 4111, Australia
E-mail: x.yao@griffith.edu.au
H. Liu, Prof. D. Yang
Collaborative Innovation Center for Marine Biomass Fibers Materials and Textiles of Shandong Province
Institute of Marine Biobased Materials
School of Environmental Science and Engineering
Qingdao University
Shandong 266071, P. R. China
Dr. R. K. Hocking
Department of Chemistry and Biotechnology
Faculty of Science, Engineering and Technology
Swinburne University of Technology
Hawthorn, Melbourne, Victoria 3122, Australia
Dr. H. Liu
Australian Centre for Microscopy & Microanalysis (ACMM)
The University of Sydney
Sydney, NSW 2006, Australia
Dr. J. Chen
Intelligent Polymer Research Institute
ARC Centre of Excellence for Electromaterials Science
AIIM Facility
University of Wollongong
Innovation Campus, Wollongong, NSW 2522, Australia
Dr. C.-L. Dong, Dr. Y.-C. Huang
Department of Physics
Tamkang University
151 Yingzhuan Road, New Taipei City, 25137 Taiwan, ROC
Dr. S. Shen
International Research Centre of Renewable Energy
State Key Laboratory of Multiphase Flow in Power Engineering
Xi'an Jiaotong University
Shaanxi 710049, P. R. China

shift reaction,[4] CO oxidation,[9,10] hydrogenation,[10,11] photochemical, and (photo)electrochemical reaction.[12–15] Besides the merit of high atom utilization efficiency in atomically dispersed catalysts, another distinct advantage is that the tuneable coordination configuration of the single atomic site can synergistically alter the reaction pathway, leading to tailored catalytic performance. However, to date the wide implementation of atomically dispersed catalysts in heterocatalysis still confront at least two obstacles: i) only low content of atomically hetero-coordinated moieties can be formed as active sites due to the extremely low loading of atomic metal species (<1.5 wt%) for avoiding the sintering issue;[16] ii) the origin of the structure–property correlation between atomically hetero-coordinated moieties and tailored activities remains ambiguous, owing to the difficulty in synthesizing and characterizing targeted coor- dinated moieties without other structural and compositional impurities.

Recently, the importance of defects in oxygen-involving electrocatalysis has been demonstrated by several groups.[17–20] For instance, the electronic state is asymmetrically tailored at the vacancy or reconstructed carbon defect sites of graphene compared to perfect hexagonal lattice, which can not only enhance the electrocatalytic activity in oxygen reduction reaction (ORR), but also be functional for other electrochemical reactions, such as oxygen evolution reaction (OER) and hydrogen evolution reaction (HER).[21] Similarly, defect-rich transition-metal oxides and TMDs (e.g., MoS_2 and $CoSe_2$) have also been demonstrated to increase their electrocatalytic activities owing to the tuned bandgaps through defect-induced crystal strain.[22,23] However, it is still a grand challenge to retain the stability of these defect sites especially under the harsh redox process of the electroca- talysis. To this end, coordination of the defect sites with metal atomic species in defect-rich carbons or TMDs may be a poten- tial strategy to stabilize the topological structures of defects, prevent atomic metal species from aggregation, and even fur- ther manipulate the local electronic distribution through the diverse coordinated configurations. In our previous study, we directly identified the coordination structure of atomic Ni trapped in graphene defects by using aberration-corrected transmission electron microscopy (TEM), and revealed that dif- ferent integrated coordination structures (atomic Ni at various carbon defects) may be the specific active sites for OER and HER, respectively.[24] With respect to the defect coordination in TMDs, Liu et al. reported that isolated Co atoms (1.8 wt%) can be stably doped on the MoS_2 monolayer via forming the Co–S–Mo coordination structure, which endows the catalyst with excellent activity, selectivity, and stability for the hydrode-
oxygenation reaction.[6] Additionally, defects on g-C N [25] and

reducible oxides (like FeO_x, CeO_2, and TiO_2)[4,26–28] have also been applied to stabilize atomically dispersed metal atoms on supports. Nevertheless, synthesizing the above atomic coordination structures normally involves sophisticated or harsh treatment process (e.g., high-temperature pyrolysis, acid leaching, and electrochemical activation), which would limit the practical application of the above catalysts. Moreover, even it is well-known that the single metal centres cannot perform catalysis alone, for the vast majority of the single atom catalysts, their real active sites have not been unambiguously revealed.[29] Therefore, it is highly desirable to design and synthesize hetero-coordinated moieties at atomic scale with definite struc- ture through a convenient strategy for raising the performance and deepening the mechanistic understanding of heteroge- neous catalysis.

It is assumed that the formation of hetero-coordinated moieties at atomic scale with asymmetrical electronic distribution should be conducive to the OER catalysis, as it can benefit the adsorption and desorption of the adsorbates.[24,30] To prove it, we design the atomically coordinated Pt–Co–Se moieties with highly asymmetrical electronic distribution for OER electrocatalysis. The hypothesis is that the lower electronic site (Co) (compared with Pt) is more attractive to OH*, and simultaneously the lower electronic site is balanced by the negative charged OH*. Afterward, the balanced electronic site (Co) is thus favorable for the OOH* desorption. We apply a facile room-temperature photochemical method (UV irradiation)[28] to prepare Pt atomically dispersed defective $CoSe_2$ nanosheets ($CoSe_{2-x}$-Pt) with a Pt loading content of 2.25 wt%. Both the X-ray absorption fine structure (XAFS) analysis and high-angle annular dark-field scanning transmission electron microscopy (HAADF-STEM) image can verify the filling of single Pt and formation of atomic Pt–Co–Se coordination. We carry out the density functional theory (DFT) calculations and use the standard deviation (σ) value of the Bader charge numbers of Se atoms as a descriptor to represent the electronic distribu- tion asymmetry degree. Owing to the formation of atomically coordinated Pt–Co–Se moieties, the σ value of $CoSe_2$ matrix significantly increases from 0.027 ($CoSe_2$-origin) to 0.070, indicating the prominently elevated electronic distribution asymmetry degree of $CoSe_{2-x}$-Pt. The superior OER performance of $CoSe_{2-x}$-Pt with high asymmetry degree supports our hypothesis. $CoSe_{2-x}$-Pt catalyst exhibits a high activity for OER in 1.0 m KOH, delivering a specific activity of 16.5 and 9.0 times greater than that of $CoSe_2$-origin and $CoSe_{2-x}$, respectively. The plasma-photochemical process can also load the single Ni and Ru atomic species on $CoSe_{2-x}$, but the OER activities of $CoSe_{2-x}$-Ni and $CoSe_{2-x}$-Ru are lower than that of $CoSe_{2-x}$-Pt, which may be attributed to their smaller electronic distribution asymmetry degree.

The $CoSe_2$-origin was synthesized in conformity to the existing literature.[31] The as-prepared $CoSe_2$-origin nanoplates (Figure S1, Supporting Information) were subjected to argon (Ar) microwave plasma treatment at 100 W for different lengths of time (30, 75, and 120 min) to obtain $CoSe_2$ nanosheets with abundant selenium vacancies ($CoSe_{2-x}$), as illustrated in **Figure 1**a. The Ar plasma treatment can successfully exfoliate the material into much thinner nanosheets (1.8 nm, 3 $CoSe_2$ layers) (Figure 1b,c; Figure S2, Supporting Information).[31]
The X-ray diffraction (XRD) patterns (Figure 1d) and Raman spectra (Figure S3, Supporting Information) both demonstrate that the exfoliation process of $CoSe_2$-origin would not alter its crystal structure.[32–34] As the $CoSe_{2-x}$-75 min shows the best OER activity among all the $CoSe_{2-x}$ samples (Figure S4, Supporting Information), $CoSe_{2-x}$-75 min was chosen as support to load the Pt atoms. H_2PtCl_6 solution was added into an aqueous dispersion of $CoSe_{2-x}$ to allow the adsorption of $PtCl_6^{2-}$ species, and then irradiated by low-intensity UV light provided by a Xenon lamp (Figure 1a). After irradiation for 10 min, the $CoSe_{2-x}$-Pt catalyst was collected and washed thoroughly with

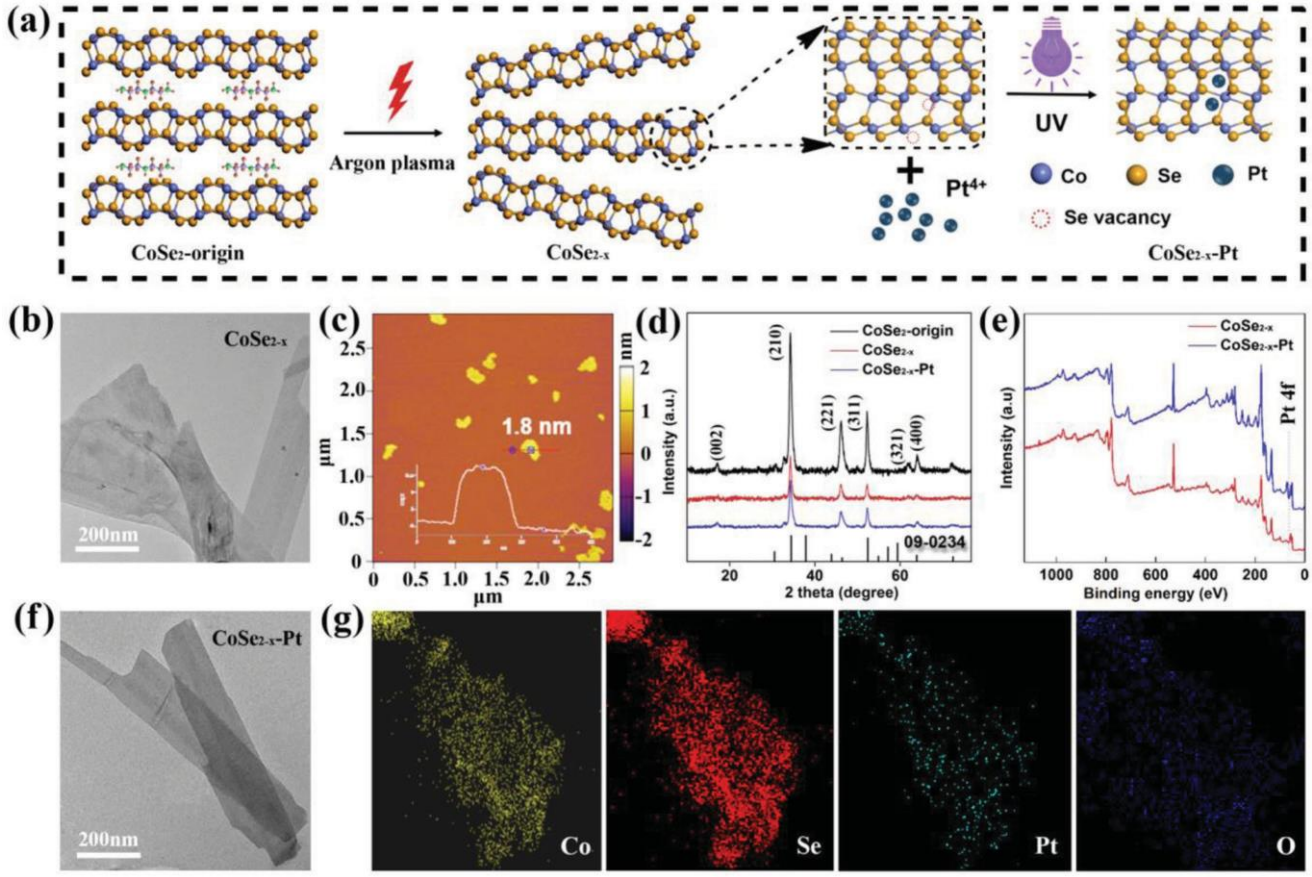

Figure 1. Preparation and morphology characterization of $CoSe_{2-x}$-Pt. a) Schematic illustration of the Ar-plasma-induced exfoliation of $CoSe_2$-origin and the loading of single Pt by UV irradiation. b) TEM image and c) AFM image of the exfoliated $CoSe_{2-x}$. d) XRD patterns of $CoSe_2$-origin, $CoSe_{2-x}$, and $CoSe_{2-x}$-Pt. e) XPS survey scan spectra of $CoSe_{2-x}$ and $CoSe_{2-x}$-Pt. f) TEM image and g) EDS mapping of $CoSe_{2-x}$-Pt.

water and ethanol. XRD pattern presents no new peak after the Pt loading (Figure 1d). However, the X-ray photoelectron spectroscopy (XPS) spectrum of $CoSe_{2-x}$-Pt shows a new peak at ≈72 eV that ascribed to Pt 4f (Figure 1e).[35] The inductively coupled plasma atomic emission spectroscopy (ICP-AES) confirms the Pt amount of $CoSe_{2-x}$-Pt to be 2.25 wt%. Importantly, even with this relatively high loading amount, no Pt nanoparticles are observed in TEM image (Figure 1f). Energy-dispersive X-ray spectroscopy (EDS) elemental mapping proves that Pt atoms are highly dispersive throughout $CoSe_{2-x}$-Pt (Figure 1g). These results trigger us to assume that the Pt species exist as single atomic species on $CoSe_{2-x}$ surface after the UV irradiation, which will be verified later.

XPS and XAFS spectroscopy were applied to study the difference on the surface of $CoSe_2$-origin and $CoSe_{2-x}$. After Ar plasma treatment, the peak of Co–Se species at 778.0 eV[36,37] in the Co 2p spectrum becomes obviously weaker (**Figure 2**a). Meanwhile, in the Co *K*-edge X-ray absorption near edge structure (XANES) spectra (Figure 2b), a substantial shift of the XANES peak to a lower energy is observed after Ar plasma exfoliation. This should be attributed to the formation of selenium vacancies.[38,39] Moreover, in the Co k^3-weighted Fourier transform extended X-ray absorption fine structure (EXAFS) spectra, the peaks at about 2.10 Å are corresponding to the Co–Se contribution (Figure 2c),[23,40,41] and the intensity decreases after Ar plasma treatment. The EXAFS data fitting results show that compared with $CoSe_2$-origin, the coordination numbers (C.N.) for Co–Se1 (the first Co–Se shell) and Co–Se2 (the second Co–Se shell) of $CoSe_{2-x}$ reduce by 1.5 and 0.5, respectively (Figure S5 and Table S1, Supporting Information).[40,42] The Se *K*-edge XANES intensity of $CoSe_{2-x}$ also obviously reduces compared with $CoSe_2$-origin (Figure S6, Supporting Information), indicating the reduction in C.N. of Se–Co because of the positive correlation of intensity with C.N.[43] These data verify the successful creation of selenium vacancies by Ar plasma.

After loading the Pt atoms, the Pt 4f XPS spectrum of $CoSe_{2-x}$-Pt can only be fitted into peaks that attributed to oxidized Pt^{2+} (Figure 2d).[35] No peak that is ascribed to the metallic clusters (Pt^0) or $PtCl_6^{2-}$ species (Pt^{4+}) can be found in the XPS spectrum. Besides, in the normalized XANES spectra of the Pt L_3-edge (Figure 2e), the white-line prominent peak intensity of $CoSe_{2-x}$-Pt is between those of Pt foil and PtO_2, suggesting the partial oxidation of Pt atoms in $CoSe_{2-x}$-Pt.[24,44] EXAFS spectra can provide important evidence on the atomic dispersion of Pt species on $CoSe_{2-x}$ (Figure 2f). No Pt□Pt contribution at about 2.60 Å can be found in the k^2-weighted EXAFS of the Pt L_3-edge for $CoSe_{2-x}$-Pt; therefore Pt should exist predomi- nantly as single atomic species on $CoSe_{2-x}$-Pt.[10] Instead, a

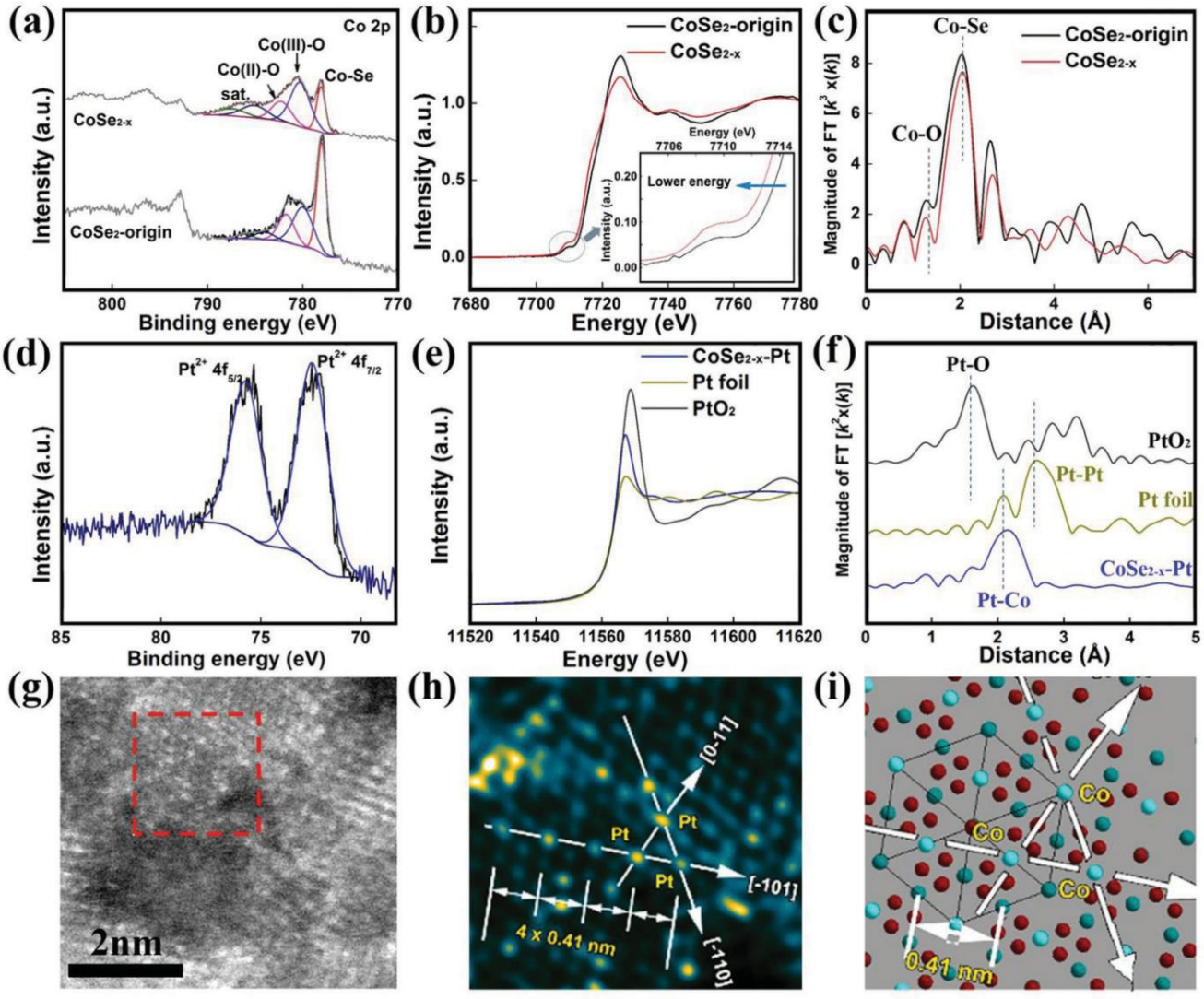

Figure 2. The structural characterizations of $CoSe_{2-x}$ and $CoSe_{2-x}$-Pt. a) High-resolution Co 2p XPS spectra of $CoSe_2$-origin and $CoSe_{2-x}$. b) Co K-edge XANES spectra and c) k^3-weighted Fourier transform EXAFS spectra of the Co for $CoSe_2$-origin and $CoSe_{2-x}$. d) High-resolution Pt 4f XPS spectrum of $CoSe_{2-x}$-Pt. e) Pt L_3-edge XANES spectra and f) k^2-weighted Fourier transform EXAFS spectra of the Pt for Pt foil, PtO_2, and $CoSe_{2-x}$-Pt. g) The unprocessed HAADF-STEM image of $CoSe_{2-x}$-Pt. The contrast is proportional to square of atomic number. The white atoms in the yellow square area correspond to heavy metal Pt atoms. h) The processed and colored HAADF-STEM image of $CoSe_{2-x}$-Pt. The bright yellow spots are Pt atoms and the cyan spots are Co atoms. i) 2D atomic arrangement of bright Co atoms on (210) plane and of dark Co and Se atoms underneath (210) plane.

prominent peak at 2.14 Å arising from Pt□Co contribution[45] can be seen in the Pt L_3-edge EXAFS spectrum of $CoSe_{2-x}$-Pt. These results confirm that the single Pt are dominantly present as atomic Pt□Co coupling at selenium vacancies of the $CoSe_2$ surface to form atomically coordinated Pt–Co–Se moieties. The C.N.s of Pt□O, Pt□Se, and Pt□Co can be fitted to 1.0, 1.0, and 2.0, respectively, by given in Figure S7 and Table S2 (Supporting Information).

The high-angle annular dark-field high-resolution transmission electron microscopy (HAADF-HRTEM) image (Figure 2g) shows that the Pt atoms, which are of higher atomic number and thus higher contrast than the sur- rounding Co atoms, homogeneously scatter across the $CoSe_2$ basal plane.[6] According to the fast Fourier transformation (FFT) (Figure S8a, Supporting Information) of the selected area in Figure 2g, as well as the corresponding lattice parameters (Figure S8b, Supporting Information), the observed basal plane can be verified to be the (210) plane of $CoSe_2$. Benefiting from the FFT and inverse FFT, noise was filtered and the colored HAADF image of $CoSe_{2-x}$-Pt clearly shows the ordered distribution of the Pt atoms with the size of ≈0.2 nm on $CoSe_2$ surface, situating on Co atop sites (Figure 2h,i). All the aforementioned results prove that single Pt are success- fully trapped by selenium vacancies to form atomically coor- dinated Pt–Co–Se moieties.

The influence of the single Pt filling on the OER performance of $CoSe_2$ matrix is investigated. It should be noted that the existence of Se vacancy is essential for the single Pt trapping. Even the same H_2PtCl_6 solution dosage is used (1.5 mL, 5.0×10^{-3} m), much more Pt species can be trapped on $CoSe_{2-x}$ (2.25 wt%)

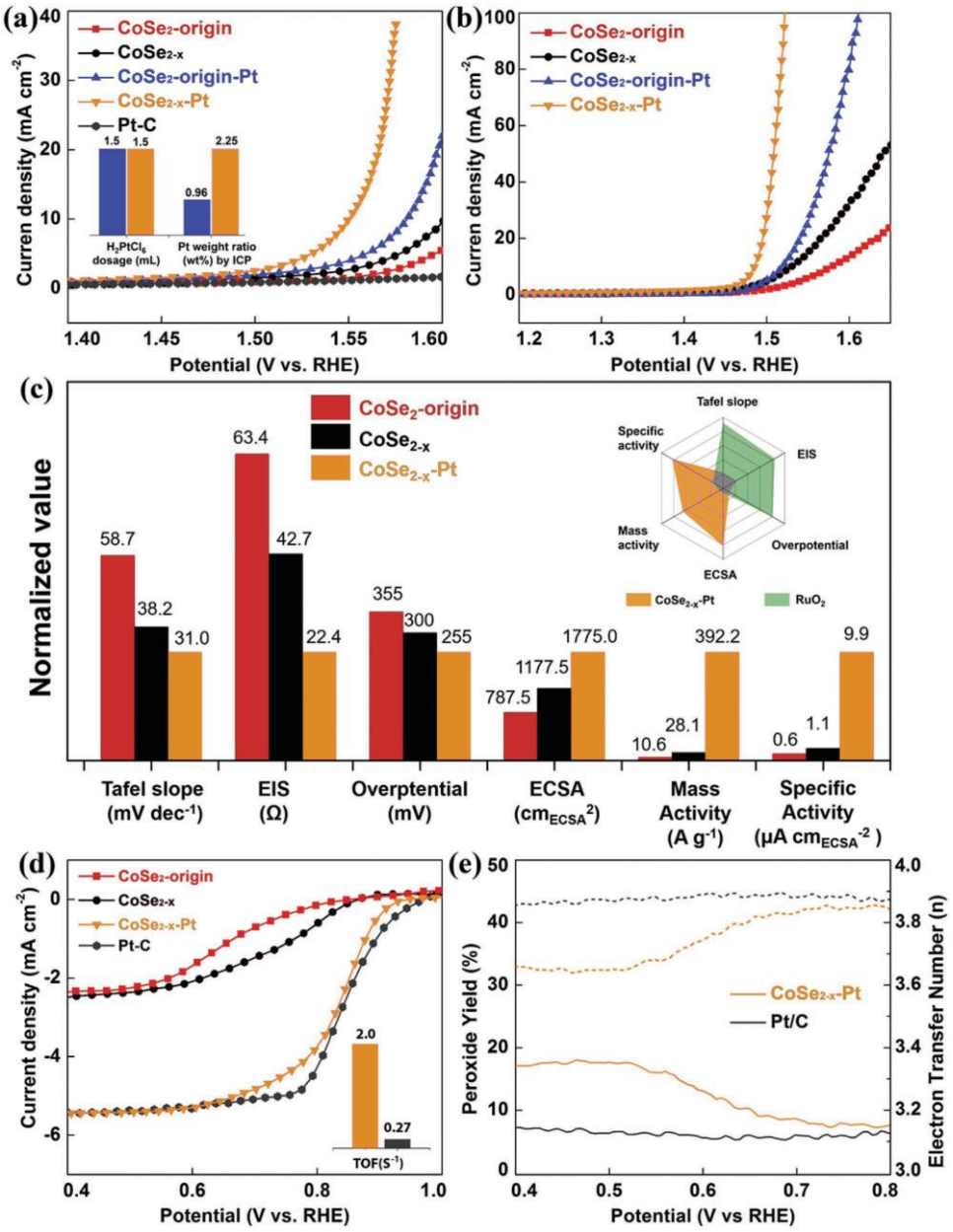

Figure 3. Electrochemical oxygen evolution and oxygen reduction activities. a) OER polarization curves of $CoSe_2$-origin, $CoSe_2$-origin-Pt, $CoSe_{2-x}$, $CoSe_{2-x}$-Pt, and 20 wt% Pt/C performed in 0.1 m KOH. b) OER polarization cures of $CoSe_2$-origin, $CoSe_2$-origin-Pt, $CoSe_{2-x}$, and $CoSe_{2-x}$-Pt performed in 1.0 m KOH. c) The comparisons of overpotential to reach a current density of 10 mA cm^{-2}, Tafel slope, EIS at a potential of 0.65 V versus Ag/AgCl, ECSA, mass activity, and specific activity at an overpotential of 300 mV among $CoSe_2$-origin, $CoSe_{2-x}$, and $CoSe_{2-x}$-Pt, and the inset shows the radar chart comparing the activity between $CoSe_{2-x}$-Pt and RuO_2 in 1.0 m KOH. d) ORR polarization cures of $CoSe_2$-origin, $CoSe_{2-x}$, $CoSe_{2-x}$-Pt, and commercial 20 wt% Pt/C performed in 0.1 m KOH, the inset shows the TOF of Pt atoms of $CoSe_{2-x}$-Pt and Pt/C. e) The percentage of peroxide yields and the electron transfer numbers of $CoSe_{2-x}$-Pt and Pt/C for ORR in 0.1 m KOH solution.

than $CoSe_2$-origin (0.96 wt%) (**Figure 3**a). Meanwhile, some Pt atoms on $CoSe_2$-origin would aggregate into Pt clusters because there are not enough selenium vacancies (Figure S9, Supporting Information). As a sequence, $CoSe_{2-x}$-Pt shows a much better OER activity than $CoSe_{2-x}$ and $CoSe_2$-origin- Pt (Figure 3a). Interestingly, the commercial Pt/C catalyst exhibits nearly no OER activity in 0.1 m KOH (Figure 3a), but here the single Pt is found to remarkably boost the OER per- formance of $CoSe_{2-x}$. Moreover, with the increase of Pt content from 0 to 2.25 wt%, the overpotential required for $CoSe_{2-x}$-Pt to reach a current density of 10 mA cm^{-2} in 0.1 m KOH significantly decreases from 370 mV to 314 mV (Figure S10a, Supporting Information), while their corresponding current density at $\eta = 350$ mV sharply increases from 4.0 to 43.0 mA cm^{-2} (Figure S10b, Supporting Information). However, when further increasing the Pt loading amount to 4.06 wt%, its cur- rent density decreases to 8.8 mA cm^{-2} (Figure S10b, Supporting Information). The HRTEM image of $CoSe_{2-x}$-Pt-4.06 wt%

shows that the Pt atoms on $CoSe_2$ surface aggregate into par- ticles with the size of ≈2.5 nm (Figure S11, Supporting Infor- mation). The notably enhanced OER catalytic performance of $CoSe_{2-x}$-Pt-2.25 wt% in comparison to $CoSe_{2-x}$-Pt-4.06 wt% confirms that the single Pt is much superior to metallic bulk Pt in improving the OER activity of $CoSe_2$ support.

Single Ni and Ru were also introduced onto the $CoSe_{2-x}$ surface through the same photochemical reduction strategy. The existence of Ni and Ru atoms on $CoSe_{2-x}$ can be con- firmed by XPS (Figure S12, Supporting Information),[46,47] while their contents are verified by ICP-AES to be 1.1 and 1.9 wt%. From the TEM images no nanoparticles can be observed on $CoSe_{2-x}$ surface (Figure S13, Supporting Information), but EDS mapping images show that Ni and Ru species are highly dispersive across the $CoSe_{2-x}$ surface (Figures S14 and S15, Supporting Information). X-ray absorption spectroscopy (XAS) measurement further verifies the single-atom state of Ni on $CoSe_{2-x}$ (Figure S16, Supporting Information). After loading the single Ni and Ru, the OER activity of $CoSe_{2-x}$ can both be improved (Figure S17a, Supporting Information). But as indicated in Figure S17b–d (Supporting Information), $CoSe_{2-x}$-Pt exhibits a much higher OER activity even at the same loading content. It implies that the coordinated Pt–Co–Se moiety is more active than Ru–Co–Se and Ni–Co–Se, even Ni and Ru are reported to be active OER active sites.[24,48] The higher reactivity should be attributed to the different electronic distribution asymmetry degree induced by single Pt, Ni, and Ru sites,[21,24] which can improve the OER activity to different extent. It will be discussed in the following DFT calculation part.

The above OER measurement was conducted in 0.1 m KOH solution. To facilitate the activity comparison of our synthe- sized $CoSe_{2-x}$-Pt with other reported catalysts,[21,49] the OER activities of the materials have also been tested in 1.0 m KOH (Figure 3b). It can be found that the $CoSe_{2-x}$-Pt requires a sig- nificantly lower overpotential (255 mV) to afford a current den- sity of 10 mA cm^{-2} than $CoSe_2$-origin (355 mV) and $CoSe_{2-x}$ (300 mV). In Figure 3c, the Tafel slopes (Figure S18, Supporting Information) and the charge transfer resistance (Figure S19, Sup- porting Information) calculated from electrical impedance spec- troscopy (EIS) both reveal a faster charge transfer in $CoSe_{2-x}$-Pt during the OER process.[37] Actually, the activity of $CoSe_{2-x}$-Pt has outperformed most of the reported $CoSe_2$-based OER cata- lysts to date and other state-of-the-art nonprecious metal cata- lysts (Table S3, Supporting Information). Through obtaining the double layer capacitances (C_{dl}) of the samples through cyclic vol- tammetry measurement (Figure S20, Supporting Information), the electrochemical active surface areas (ECSAs) of $CoSe_{2-x}$-Pt, $CoSe_2$-origin, and $CoSe_{2-x}$ can be estimated to be 1775.0, 787.5, and 1177.5 cm_{ECSA}^{2}, respectively.[50] When normalizing the OER mass activity of the catalysts to the ECSA, it can be found that the specific activity of $CoSe_{2-x}$-Pt (9.9 μA cm_{ECSA}^{-2}) is 16.5 times and 9.0 times greater than that of $CoSe_2$-origin (0.6 μA cm_{ECSA}^{-2}) and $CoSe_{2-x}$ (1.1 μA cm_{ECSA}^{-2}) (Figure 3c). The CoSe -Pt shows an activity far better than the commercial precious RuO_2 catalyst (as seen in the inset radar chart of Figure 3c). Besides, the Faradaic efficiency of $CoSe_{2-x}$-Pt in 1.0 m KOH is calculated as 96.1%, and no CO and CO_2 were detected in its OER product (Figure S21, shows a promising OER stability in 1.0 m KOH. During the 10 000 s of stability test at a constant overpotential of 250 mV, its current density shows negligible decrease (Figure S22, Sup- porting Information). After the OER test, XRD and TEM tests prove no obvious change on the structure of $CoSe_{2-x}$-Pt (Figure S23, Supporting Information). Meanwhile, Co *K*-edge XANES and k^3-weighted Fourier transform EXAFS spectra verify that the cubic crystal structure of $CoSe_2$ can be maintained in the OER reaction. Pt L_3-edge XANES spectra and k^2-weighted Fourier transform EXAFS spectra of $CoSe_{2-x}$-Pt-after OER prove that Pt atoms would be mildly oxidized in the OER reaction, but still keep as the form of single atomic species on $CoSe_{2-x}$ (Figure S24, Supporting Information). All these results demonstrate that single Pt can be stabilized by forming the atomically coordinated Pt–Co–Se moieties even in the harsh reaction condition.

Then we investigated the catalytic oxygen reduction (ORR) by the synthesized $CoSe_{2-x}$-Pt catalyst. As shown in Figure 3d, $CoSe_{2-x}$-Pt exhibits a remarkably higher half-wave potential (0.83 V vs reversible hydrogen eletrode (RHE)) than $CoSe_2$- origin (0.64 V vs RHE) and $CoSe_{2-x}$ (0.75 V vs RHE), as well as much larger limit current density. Even the half-wave poten- tial of $CoSe_{2-x}$-Pt is still slightly inferior to that of commercial 20 wt% Pt/C catalyst (0.85 V vs RHE), the turnover frequency (TOF) of Pt atoms in $CoSe_{2-x}$-Pt (2.0 s^{-1}) is 7.4 times greater than that of Pt/C (0.27 s^{-1}). The atomically coordinated Pt– Co–Se moieties can even alter the ORR reaction pathway of single Pt. Based on the Koutecky–Levich plots (Figure S25, Sup- porting Information) and ring-disk currents (Figure 3e), the electron transfer number (*n*) of $CoSe_{2-x}$-Pt is calculated to be larger than 3.6, implying its $4e^-$ transfer pathway for ORR.[51] It is well-known that the O□O dissociation is the key step of the $4e^-$ pathway. Because of the kinetic barrier of O□O disso- ciation,[52] the isolated single Pt often activates a $2e^-$ pathway and generates H_2O_2 as the ORR product.[24] However, the $CoSe_{2-x}$-Pt undergoes a distinct $4e^-$ pathway in contrast to iso- lated Pt atoms, indicating that the Pt□Co interaction could play a key role to break the O□O bond and activate the ORR in a $4e^-$ pathway. Instead, the loading of single Ni and Ru on $CoSe_{2-x}$ would be not beneficial for ORR, leading to the decrease of the activity (Figure S26, Supporting Information).

Figure S27 (Supporting Information) clearly represents the good OER/ORR bifunctional activities of $CoSe_{2-x}$-Pt in 0.1 m KOH, with a small potential difference of 0.73 V between the OER potential for 10.0 mA cm^{-2} and ORR half-wave potential. This potential difference is even smaller than that of the control catalyst mixed by Pt/C (for ORR) and RuO_2 (for OER) (0.77 V) and other reported ORR/OER bifunctional catalysts (Figure S28, Supporting Information). After assembling the $CoSe_{2-x}$-Pt catalyst into a rechargeable Zn–air battery (Figure S29a,b, Supporting Infor- mation), it delivers a current density of 101 mA mg^{-1} at the dis- charge voltage of 1.0 V, and a peak power density of 155 mW mg^{-1} at a current density of 280 mA mg^{-1} (Figure S29c, Supporting Information). Moreover, $CoSe_{2-x}$-Pt exhibits a promising durability Supporting Information), confirming that almost all the electrons can be involved in its OER process. Moreover, the $CoSe_{2-x}$-Pt

at current densities of 5.0 mA mg^{-1} (Figure S29d, Supporting Infor- mation). After 780 charge/discharge cycles (300 s per cycle), the charge potentials still hold at 2.0 V, while the discharge potentials only decline slightly to 1.2 V. Besides, as a demonstration shown in Figure S29e (Supporting Information), two Zn–air batteries can be connected in series to power a light-emitting diode light (≈2 V).

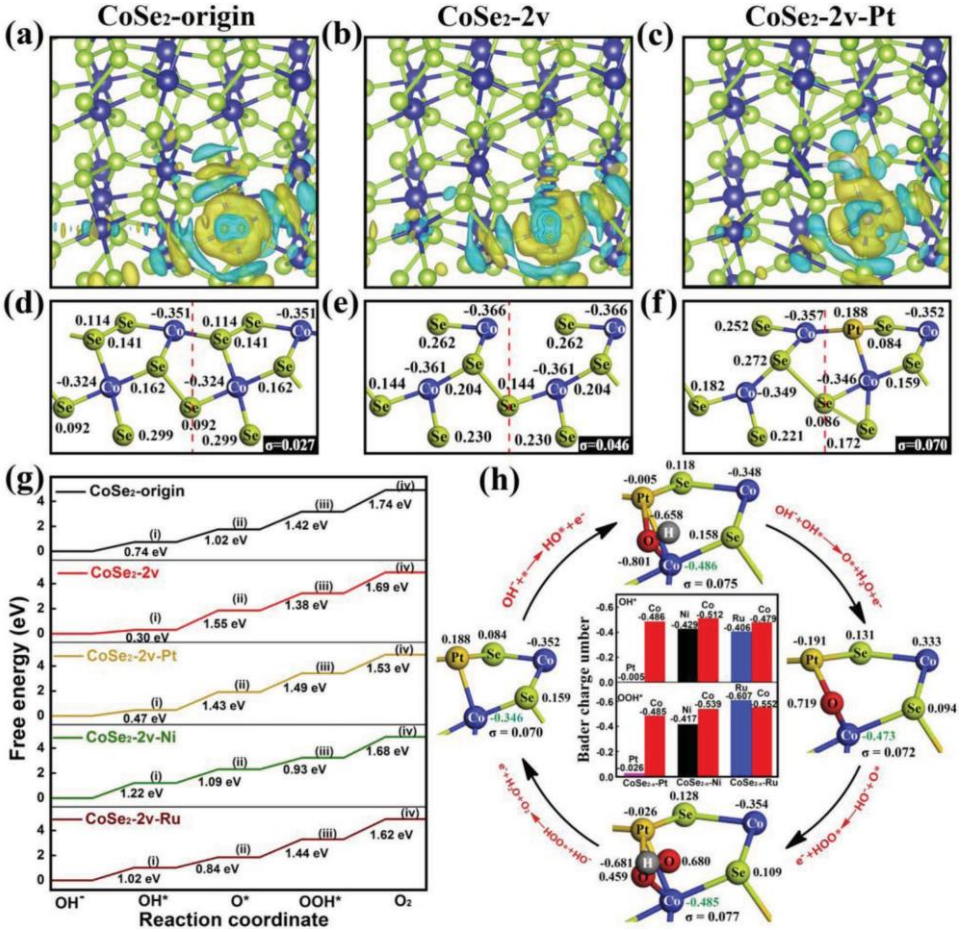

Figure 4. Mechanistic study of catalytic active sites on $CoSe_{2-x}$-Pt. a–c) The geometries of $CoSe_2$-origin, $CoSe_{2-x}$, and $CoSe_{2-x}$-Pt and their 3D charge density differences calculated by DFT. d–f) The Bader charge numbers of atoms in $CoSe_2$-origin, $CoSe_{2-x}$, and $CoSe_{2-x}$-Pt. The different colors represent the different charge numbers. g) Energy profiles of the $CoSe_2$-origin, $CoSe_{2-x}$, $CoSe_{2-x}$-Pt, $CoSe_{2-x}$-Ni, and $CoSe_{2-x}$-Ru for OER. h) The Bader charge numbers of atoms of $CoSe_{2-x}$-Pt during the OH*, O* and OOH* adsorption, and OOH* desorption process. The inset shows the comparison of Bader charge number of M (Pt, Ni, and Ru) and Co atoms in $CoSe_{2-x}$-Pt, $CoSe_{2-x}$-Ni, and $CoSe_{2-x}$-Ru after OH* and OOH* adsorption.

Based on the above experimental data, we attribute the remarkably enhanced OER activities of $CoSe_{2-x}$-Pt to the formation of atomically coordinated Pt–Co–Se moiety structure. To reveal its role in improving the OER performance of $CoSe_2$, a series of DFT calculations were conducted (see computational details in the Supporting Information). **Figure 4**a–c shows the 3D charge density differences of $CoSe_2$-origin, $CoSe_{2-x}$, and $CoSe_{2-x}$-Pt. Two Se atoms are removed from the structure model of $CoSe_2$-origin to form the stable structure of $CoSe_{2-x}$ ($CoSe_2$-2v). With the removal of two Se atoms, the electrons that previously occupied Se 4p orbitals become delocalized around the Co atoms neighboring the selenium vacancies, as well as the adjacent Se atoms.[53] Moreover, after loading the Pt atoms to the vacancies, the charge will be further deviated owing to the difference of the electronegativity among Pt (2.28), Se (2.55), and Co (1.88). Therefore, compared with $CoSe_2$-origin (Figure 4a), the electrons are more inclined to redistribute and accumulate around the selenium vacancies (Figure 4b), and even more around atomically coordinated Pt–Co–Se moieties (Figure 4c), leading to a significantly increased electronic distribution asymmetry degree.[24,30] We calculate the Bader charge numbers of the atoms, and use the standard deviation (σ) of the charge numbers of Se atoms as a descriptor to quantify the asymmetry degree. As shown in Figure 4d–f, the Co atom would lose electrons (negative value), while the Se atoms would obtain electrons (positive value). For $CoSe_2$-origin (Figure 4d), its overall electron distribution is nearly symmetric; thus the σ value of $CoSe_2$-origin is as low as 0.027. The σ value could increase to 0.046 and further to 0.070 after introducing the Se vacancies (Figure 4e) and loading the single Pt (Figure 4f), respectively. The different electronic distribution asymmetry degree could affect the local density of states (LDOS) of the materials. As shown in Figure S30 (Supporting Information), the 3d-orbitals of Co atoms and 2p-orbitals of Se atoms of $CoSe_{2-x}$-Pt show much higher LDOS near Fermi level than $CoSe_2$-origin and $CoSe_{2-x}$. According to the d-band centre theory, the d-band of substrate could interact strongly with the highest occupied molecular orbital and lowest unoccupied molecular orbital of the adsorbate, and the higher electron density near the Fermi level will facilitate the adsorption of adsorbates.[24,54]

The key to a high OER activity is an appropriate interaction strength between the active sites and reaction intermediates.[55]

To demonstrate the change of the electronic distribution asymmetry degree of the materials on the interaction between the Co sites and OER intermediates, the Bader charge numbers of the coordinated sites during OH*, O*, and OOH* adsorption (Figures S31–S33, Supporting Information), and the standard free-energy diagram for OER of the materials at zero poten- tial are calculated (Figure 4g). For $CoSe_2$-origin, as no delo- calized electrons exist (low asymmetry degree), the Co atom needs to directly transfer electrons to the adjacent Se atoms, as well as the adsorbed OH* (Figure S31, Supporting Informa- tion). Therefore, the interaction between OH* and Co sites is weak, and OH* adsorption energy on $CoSe_2$-origin reaches to 0.74 eV. With the transformation from OH* to O*, and further to OOH*, the Co atom of $CoSe_2$-origin would continuously transfer electrons to the intermediates, and its Bader charge number increases up to −0.590 e (Figure S31, Supporting Information). For this reason, the interaction between Co atom and adsorbed OOH* would be excessively strong, and hinder the following desorption of OOH*, which can be proved by its high free energy barrier (1.74 eV). Since the OOH* to O_2 step is the rate-determining step for all the $CoSe_2$ samples in this work, this large free energy barrier indicates its poor OER activity. For $CoSe_2$-2v, even Co atom needs to transfer more electrons to adjacent Se atoms because of two selenium vacancies (high asymmetry degree), the delocalized electrons around the Co atom neighboring selenium vacancies can help to strongly adsorb the OH*, and decrease the OH* adsorption energy to 0.30 eV. But this interaction may be too strong, and hinder the following OH* and O* transformation, as well as OOH* desorption (Figure S32, Supporting Information). The free energy barrier of the OOH* desorption step for $CoSe_2$-2v is still up to 1.69 eV. With respect to $CoSe_2$-2v-Pt, though the electronegativity of Pt (2.28) is smaller than that of Se atom (2.55), and needs to transfer electrons to OH* and adjacent Se atoms, it is high enough for Pt atom to attract electrons from the delocalized electron cloud. Therefore, after OH* adsorption the Bader charge number of Co atom reaches to −0.486 e, while that of Pt atom is only −0.005 e (Figure 4h; Figure S33, Supporting Information). The significantly lower electronic site (Co) (compared with Pt) is more attractive to OH*, and simultaneously the lower electronic site is balanced by the negative charged OH*. Hence, the adsorption energy of OH* is quite appropriate (0.47 eV) (Figure 4g). It can avoid the issue of weak intermediate adsorption that would result in an inferior reaction efficiency (overhigh adsorption energy), as well as excessively strong intermediate binding that would occupy all the available surface sites and poison the reactive surface (overlow adsorption energy). The highly asymmetrical electron cloud induced by selenium vacancies and single Pt can further transfer electrons to the intermediates during the OH* and O* transformation, and OOH* desorption process to keep the Bader charge number of Co under −0.500 e, so as to avoid excessively strong intermediate binding (Figure 4h). In this way the free energy barrier of OOH* desorption can be significantly decreased to 1.53 eV. Single Pt is theoretically proved to greatly improve the OER activity of $CoSe_2$ matrix (Figure 4g).

The electronegativities of Ni (1.91) and Ru (2.20) are also smaller than that of Se (2.55), and thus electrons of Ni and Ru atoms prefer to accumulate on the Se atoms when they coordinate. Meanwhile, they are smaller than that of Pt (2.28), so that single Ni and Ru cannot attract electrons from delocalized electron cloud as efficiently as single Pt. Consequently, the loading of single Ni and Ru atoms on selenium vacancies can only increase the σ value of $CoSe_2$ to 0.052 and 0.058, respectively (Figures S34 and S35, Supporting Information), obviously lower than that of $CoSe_2$-2v-Pt. Even they still can enhance the interaction between the Co sites and the adsorbates, the Gibbs free energy barriers of $CoSe_{2-x}$-Ni and $CoSe_{2-x}$-Ru are 1.68 and 1.62 eV (Figure 4g), respectively, indicating their inferior OER activities to $CoSe_{2-x}$-Pt (1.53 eV). To better explain the effect of M type (M = Pt, Ni, and Ru) on the OER activity of the $CoSe_{2-x}$-M catalysts, we specifically compare the Bader charge numbers of M and Co atoms of these catalysts after OH* and OOH* adsorption (Figure 4h; Figures S36 and S37, Supporting Information). Because of the various electronegativity, after the OH* adsorption, the Bader charge number difference of Co (−0.512 e) and Ni (−0.429 e) atoms in $CoSe_{2-x}$-Ni, and that of Co (−0.479 e) and Ru (−0.406 e) in $CoSe_{2-x}$-Ru is much smaller than that between Co and Pt atoms (Figure 4h; Figures S36 and S37, Supporting Information). Therefore, the electronic site of Co atoms in $CoSe_{2-x}$-Ni and $CoSe_{2-x}$-Ru cannot be balanced by the negative charged OH* as effectively as that in $CoSe_{2-x}$-Pt, which is not favorable for OH* adsorption on Co sites. The OH* adsorption free energies on $CoSe_{2-x}$-Ni and $CoSe_{2-x}$-Ru are 1.22 and 1.02 eV (Figure 4g), respectively.[56] But after OOH* adsorption, the Co and Ni Bader charge numbers of $CoSe_{2-x}$-Ni would be remarkably increased to −0.539 e and −0.417 e, while Co and Ru Bader charge numbers of $CoSe_{2-x}$-Ru to −0.552 e and −0.607 e (Figure 4h; Figures S36 and S37, Supporting Information), and thus OOH* would be over strongly bound on the $CoSe_{2-x}$-Ni and $CoSe_{2-x}$-Ru surfaces. Accordingly, the OOH* desorption free energies of $CoSe_{2-x}$-Ni and $CoSe_{2-x}$-Ru are as high as 1.68 and 1.62 eV, much higher than that of $CoSe_{2-x}$-Pt (1.53 eV). These calculation results strongly support the experimental results. They verify that single metal atoms inside the $CoSe_2$ defect could induce electronic distribution asymmetry, and the higher electronic distribution asymmetry induced by single Pt can significantly improve the OER activity of $CoSe_{2-x}$-Pt.

To summarize, single Pt trapped in selenium vacancies on $CoSe_{2-x}$ surface ($CoSe_{2-x}$-Pt) with a Pt loading content of 2.25 wt% can be synthesized through ultraviolet irradia- tion. XAFS proves that the selenium vacancies created by Ar plasma can stabilize the single Pt to form atomically coordinated Pt–Co–Se moiety. HAADF-STEM confirmed the ordered dispersion of single Pt on the Co atop sites of $CoSe_2$ surface. The DFT calculations demonstrate that the filling of single Pt could induce highly asymmetrical electronic distribution on $CoSe_2$ matrix, leading to its remarkably improved OER catalytic activity. Because of the significantly higher electronic distribution asymmetry degree, $CoSe_{2-x}$-Pt shows much better OER performance than $CoSe_{2-x}$-Ni and $CoSe_{2-x}$-Ru, in spite that Pt in general shows no intrinsic OER activity. Meanwhile, the formation of atomically coordinated Pt–Co–Se moieties could lead to its high selectivity for $4e^-$ pathway in ORR ($n > 3.6$), while isolated single Pt atoms normally result in a $2e^-$ pathway. This work verifies the importance of highly asymmetrical electronic distribution on the performance of electrocatalysts in

combination of experimental and theoretical methods. For a broader interest, it also proposes a general approach for stabilizing a guest atomic metal species at reaction interface of host matrix (like metal selenides and metal sulphides), paving a new route for the development of highly active and stable electrocatalysts.

Acknowledgements

L.Z. and Y.J. contributed equally to this work. L.Z. acknowledges the support from International Postgraduate Research Scholarship (IPRS) and UQ Centennial Scholarship (UQCent). Y.J. thanks Australian Research Council (ARC) Discovery Early Career Researcher Award (Grant No. DE180101030). Z.Z. would like to thank ARC Future Fellowship grant (Grant No. FT120100720) and ARC Discovery grant (Grant No. DP170104660). X.Y. thanks the financial support of ARC DP170103317. The authors also acknowledge the scientific and technical assistance of the Australian Microscopy and Microanalysis Research Facility at the UQ Centre. The authors thank the Taiwan National Synchrotron Radiation Research Center for XAFS equipment access.

Conflict of Interest

The authors declare no conflict of interest.

Keywords

asymmetrical electronic distribution, atomic metal species, oxygen evolution, selenium vacancies, synergetic interaction

Received: August 27, 2018
Revised: October 10, 2018
Published online: November 28, 2018

[1] X. Fan, G. Zhang, F. Zhang, *Chem. Soc. Rev.* **2015**, *44*, 3023. [2] F. Zaera, *Chem. Soc. Rev.* **2013**, *42*, 2746.
[3] X.-F. Yang, A. Wang, B. Qiao, J. Li, J. Liu, T. Zhang, *Acc. Chem. Res.* **2013**, *46*, 1740.
[4] J. Lin, A. Wang, B. Qiao, X. Liu, X. Yang, X. Wang, J. Liang, J. Li, J. Liu, T. Zhang, *J. Am. Chem. Soc.* **2013**, *135*, 15314.
[5] C. K. Poh, S. H. Lim, J. Lin, Y. P. Feng, *J. Phys. Chem. C* **2014**, *118*, 13525.
[6] G. Liu, A. W. Robertson, M. M. Li, W. C. H. Kuo, M. T. Darby, M. H. Muhieddine, Y. C. Lin, K. Suenaga, M. Stamatakis, J. H. Warner, S. C. E. Tsang, *Nat. Chem.* **2017**, *9*, 810.
[7] J. D. Kistler, N. Chotigkrai, P. Xu, B. Enderle, P. Praserthdam, C. Y. Chen, N. D. Browning, B. C. Gates, *Angew. Chem., Int. Ed.* **2014**, *53*, 8904.
[8] K. Jiang, S. Siahrostami, T. Zheng, Y. Hu, S. Hwang, E. Stavitski, Y. Peng, J. Dynes, M. Gangisetty, D. Su, K. Attenkofer, H. Wang, *Energy Environ. Sci.* **2018**, *11*, 893.
[9] B. Qiao, A. Wang, X. Yang, L. F. Allard, Z. Jiang, Y. Cui, J. Liu, J. Li, T. Zhang, *Nat. Chem.* **2011**, *3*, 634.
[10] Z. Zhang, Y. Zhu, H. Asakura, B. Zhang, J. Zhang, M. Zhou, Y. Han, T. Tanaka, A. Wang, T. Zhang, N. Yan, *Nat. Commun.* **2017**, *8*, 16100.
[11] H. Yan, H. Cheng, H. Yi, Y. Lin, T. Yao, C. Wang, J. Li, S. Wei, J. Lu, *J. Am. Chem. Soc.* **2015**, *137*, 10484.
[12] X. Li, W. Bi, L. Zhang, S. Tao, W. Chu, Q. Zhang, Y. Luo, C. Wu, Y. Xie, *Adv. Mater.* **2016**, *28*, 2427.
[13] C. Zhang, J. Sha, H. Fei, M. Liu, S. Yazdi, J. Zhang, Q. Zhong, X. Zou, N. Zhao, H. Yu, Z. Jiang, E. Ringe, B. I. Yakobson, J. Dong, D. Chen, J. M. Tour, *ACS Nano* **2017**, *11*, 6930.
[14] P. Yin, T. Yao, Y. Wu, L. Zheng, Y. Lin, W. Liu, H. Ju, J. Zhu, X. Hong, Z. Deng, G. Zhou, S. Wei, Y. Li, *Angew. Chem., Int. Ed.* **2016**, *55*, 10800.
[15] J. Deng, H. Li, J. Xiao, Y. Tu, D. Deng, H. Yang, H. Tian, J. Li, P. Ren, X. Bao, *Energy Environ. Sci.* **2015**, *8*, 1594.
[16] H. Li, L. Wang, Y. Dai, Z. Pu, Z. Lao, Y. Chen, M. Wang, X. Zheng, J. Zhu, W. Zhang, R. Si, C. Ma, J. Zeng, *Nat. Nanotechnol.* **2018**, *13*, 411.
[17] Y. Jia, J. Chen, X. Yao, *Mater. Chem. Front.* **2018**, *2*, 1250.
[18] C. Tang, H. F. Wang, Q. Zhang, *Acc. Chem. Res.* **2018**, *51*, 881.
[19] S. Dou, L. Tao, R. Wang, S. El Hankari, R. Chen, S. Wang, *Adv. Mater.* **2018**, *30*, 1705850.
[20] Q. Wu, L. Yang, X. Wang, Z. Hu, *Acc. Chem. Res.* **2017**, *50*, 435.
[21] Y. Jia, L. Zhang, A. Du, G. Gao, J. Chen, X. Yan, C. L. Brown, X. Yao, *Adv. Mater.* **2016**, *28*, 9532.
[22] J. Hong, C. Jin, J. Yuan, Z. Zhang, *Adv. Mater.* **2017**, *29*, 1606434.
[23] Y. Liu, H. Cheng, M. Lyu, S. Fan, Q. Liu, W. Zhang, Y. Zhi, C. Wang, C. Xiao, S. Wei, B. Ye, Y. Xie, *J. Am. Chem. Soc.* **2014**, *136*, 15670.
[24] L. Zhang, Y. Jia, G. Gao, X. Yan, N. Chen, J. Chen, M. T. Soo, B. Wood, D. Yang, A. Du, X. Yao, *Chem* **2018**, *4*, 285.
[25] Y. Zheng, Y. Jiao, Y. Zhu, Q. Cai, A. Vasileff, L. H. Li, Y. Han, Y. Chen, S. Z. Qiao, *J. Am. Chem. Soc.* **2017**, *139*, 3336.
[26] F. Dvorak, M. Farnesi Camellone, A. Tovt, N. D. Tran, F. R. Negreiros, M. Vorokhta, T. Skala, I. Matolinova, J. Myslivecek, V. Matolin, S. Fabris, *Nat. Commun.* **2016**, *7*, 10801.
[27] J. Jones, H. Xiong, A. T. DeLaRiva, E. J. Peterson, H. Pham, S. R. Challa, G. Qi, S. Oh, M. H. Wiebenga, X. I. P. Hernández, Y. Wang, A. K. Datye, *Science* **2016**, *353*, 150.
[28] P. Liu, Y. Zhao, R. Qin, S. Mo, G. Chen, L. Gu, D. M. Chevrier, P. Zhang, Q. Guo, D. Zang, B. Wu, G. Fu, N. Zheng, *Science* **2016**, *352*, 797.
[29] A. Wang, J. Li, T. Zhang, *Nat. Rev. Chem.* **2018**, *2*, 65.
[30] F. Banhart, J. Kotakoshi, A. V. Krasheninnikov, *ACS Nano* **2011**, *5*, 26.
[31] M.-R. Gao, W.-T. Yao, H. B. Yao, S.-H. Yu, *J. Am. Chem. Soc.* **2009**, *131*, 7486.
[32] Y. R. Zheng, M. R. Gao, Q. Gao, H. H. Li, J. Xu, Z. Y. Wu, S. H. Yu, *Small* **2015**, *11*, 182.
[33] M.-R. Gao, X. Cao, Q. Gao, Y.-F. Xu, Y.-R. Zheng, J. Jiang, S.-H. Yu, *ACS Nano* **2014**, *8*, 3970.
[34] C. Guan, A. Sumboja, H. Wu, W. Ren, X. Liu, H. Zhang, Z. Liu, C. Cheng, S. J. Pennycook, J. Wang, *Adv. Mater.* **2017**, *29*, 1704117.
[35] S. Takahashi, N. Takahashi, N. Todoroki, T. Wadayama, *ACS Omega* **2016**, *1*, 1247.
[36] B. Zhang, H. Chen, Q. Daniel, B. Philippe, F. Yu, M. Valvo, Y. Li, R. B. Ambre, P. Zhang, F. Li, H. Rensmo, L. Sun, *ACS Catal.* **2017**, *7*, 6311.
[37] L. Zhuang, L. Ge, Y. Yang, M. Li, Y. Jia, X. Yao, Z. Zhu, *Adv. Mater.* **2017**, *29*, 1606793.
[38] Z. Cai, Y. Bi, E. Hu, W. Liu, N. Dwarica, Y. Tian, X. Li, Y. Kuang, Y. Li, X.-Q. Yang, H. Wang, X. Sun, *Adv. Energy Mater.* **2018**, *8*, 1701694.
[39] R. K. Hocking, R. Brimblecombe, L. Y. Chang, A. Singh, M. H. Cheah, C. Glover, W. H. Casey, L. Spiccia, *Nat. Chem.* **2011**, *3*, 461.
[40] K. Xu, H. Cheng, H. Lv, J. Wang, L. Liu, S. Liu, X. Wu, W. Chu, C. Wu, Y. Xie, *Adv. Mater.* **2018**, *30*, 1703322.

[41] Y. Sun, X. Zhang, B. Mao, M. Cao, *Chem. Commun.* **2016**, *52*, 14266.
[42] S. Gao, Z. Sun, W. Liu, X. Jiao, X. Zu, Q. Hu, Y. Sun, T. Yao, W. Zhang, S. Wei, Y. Xie, *Nat. Commun.* **2017**, *8*, 14503.
[43] J. Phibbs, E. Franz, D. Hauck, M. Gallego, J. J. Tse, I. J. Pickering, K. Liber, D. M. Janz, *Ecotoxicol. Environ. Saf.* **2011**, *74*, 1855.
[44] J. Liu, M. Jiao, L. Lu, H. M. Barkholtz, Y. Li, Y. Wang, L. Jiang, Z. Wu, D. J. Liu, L. Zhuang, C. Ma, J. Zeng, B. Zhang, D. Su, P. Song, W. Xing, W. Xu, Y. Wang, Z. Jiang, G. Sun, *Nat. Commun.* **2017**, *8*, 15938.
[45] A. I. Figueroa, J. Bartolomé, L. M. García, F. Bartolomé, O. Bunău, J. Stankiewicz, L. Ruiz, J. M. González-Calbet, F. Petroff, C. Deranlot, S. Pascarelli, P. Bencok, N. B. Brookes, F. Wilhelm, A. Smekhova, A. Rogalev, *Phys. Rev. B* **2014**, *90*. 174421.
[46] L.-A. Stern, L. Feng, F. Song, X. Hu, *Energy Environ. Sci.* **2015**, *8*, 2347.
[47] M. Zhang, W. Chen, S.-J. Ding, Z.-Y. Liu, Y. Huang, Z.-W. Liao, D. W. Zhang, *J. Phys. D: Appl. Phys* **2008**, *41*, 032007.
[48] Y. Lee, J. Suntivich, K. J. May, E. E. Perry, Y. Shao-Horn, *J. Phys. Chem. Lett.* **2012**, *3*, 399.
[49] Y. Jia, L. Zhang, G. Gao, H. Chen, B. Wang, J. Zhou, M. T. Soo, M. Hong, X. Yan, G. Qian, J. Zou, A. Du, X. Yao, *Adv. Mater.* **2017**, *29*, 1700017.
[50] L. Zhuang, Y. Jia, T. He, A. Du, X. Yan, L. Ge, Z. Zhu, X. Yao, *Nano Res.* **2018**, *11*, 3509.
[51] H. W. Liang, X. Zhuang, S. Bruller, X. Feng, K. Mullen, *Nat. Commun.* **2014**, *5*, 4973.
[52] S. Yang, Y. J. Tak, J. Kim, A. Soon, H. Lee, *ACS Catal.* **2017**, *7*, 1301.
[53] Y. Wang, T. Zhou, K. Jiang, P. Da, Z. Peng, J. Tang, B. Kong, W.-B. Cai, Z. Yang, G. Zheng, *Adv. Energy Mater.* **2014**, *4*, 1400696.
[54] M. Gajdo, A. Eichler, J. Hafner, *J. Phys.: Condens. Matter* **2004**, *16*, 1141.
[55] Y. Guo, K. Xu, C. Wu, J. Zhao, Y. Xie, *Chem. Soc. Rev.* **2015**, *44*, 637.
[56] B. Zhang, X. Zheng, O. Voznyy, R. Comin, M. Bajdich, M. Garcia-Melchor, L. Han, J. X. Xu, M. Liu, L. Zheng, F. P. Garcia de Arquer, C. T. Dinh, F. Fan, M. Yuan, E. Yassitepe, N. Chen, T. Regier, P. Liu, Y. Li, P. D. Luna, A. Janmohamed, H. Xin, H. Yang, A. Vojvodic, E. H. Sargent, *Science* **2016**, *352*, 333.